Transport Studies of Dual-Gated ABC and ABA Trilayer Graphene: Band Gap Opening and Band Structure Tuning in Very Large Perpendicular Electric Fields

5 AUTHORS, INCLUDING:

Kaiqi Zou

57 PUBLICATIONS   709 CITATIONS

SEE PROFILE

Allan H Macdonald

University of Texas at Austin

664 PUBLICATIONS   10,379 CITATIONS

SEE PROFILE

Transport Studies of Dual-Gated ABC and ABA Trilayer Graphene: Band Gap Opening and Band Structure Tuning in Very Large Perpendicular Electric Fields

K. Zou,*[†,‡] Fan Zhang,[§] C. Clapp,[∥] A. H. MacDonald,[⊥] and J. Zhu[†,#]

[†]Department of Physics, The Pennsylvania State University, University Park, Pennsylvania 16802, United States
[‡]Department of Applied Physics, Yale University, New Haven, Connecticut 06511, United States
[§]Department of Physics and Astronomy, University of Pennsylvania, Philadelphia, Pennsylvania 19104, United States
[∥]Department of Chemistry, Amherst College, Amherst, Massachusetts 01002, United States
[⊥]Department of Physics, The University of Texas at Austin, Austin, Texas 78701, United States
[#]Materials Research Institute, The Pennsylvania State University, University Park, Pennsylvania 16802, United States

S *Supporting Information*

ABSTRACT: We report on the transport properties of ABC and ABA stacked trilayer graphene using dual, locally gated field effect devices. The high efficiency and large breakdown voltage of the HfO_2 top and bottom gates enable independent tuning of the perpendicular electric field and the Fermi level over an unprecedentedly large range. We observe a resistance change of 6 orders of magnitude in the ABC trilayer, which demonstrates the opening of a band gap. Our data suggest that the gap saturates at a large displacement field of $D \sim 3$ V/nm, in agreement with self-consistent Hartree calculations. In contrast, the ABA trilayer remains metallic even under a large perpendicular electric field. Despite the absence of a band gap, the band structure of the ABA trilayer continues to evolve with increasing D. We observe signatures of two-band conduction at large D fields. Our self-consistent Hartree calculation reproduces many aspects of the experimental data but also points to the need for more sophisticated theory.

KEYWORDS: *Trilayer graphene, stacking dependence, electrical transport, tunable band gap, two-band transport, self-consistent Hartree screening*
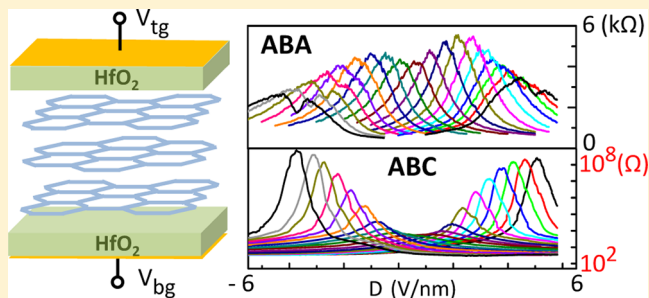
Progress in studies of graphene and its few-layer siblings has brought the potential of stacking-structure engineering of two-dimensional materials into sharp focus. For example, isolated graphene layers are gapless semiconductors with linear band crossing,[1] whereas Bernal stacked bilayer graphene has hyperbolic bands[1−4] with an electric-field tunable band gap.[5,6] Trilayer graphene possesses two stable stacking orders: ABA (Bernal) and ABC (rhombohedral) stacking, which have distinct electronic properties that are of interest both for fundamental science and for technological applications.[7−23] The conduction and valence band dispersions of ABC-trilayer graphene (ABC-TG) are expected to be approximately cubic and to touch at the charge neutrality point (CNP).[8,12] The associated divergent density of states leads to an interaction-driven symmetry broken ground state.[13] In the presence of a perpendicular magnetic field, the approximate 12-fold degeneracy of the zeroth Landau level is expected to be lifted by interactions.[18,19,21] From the technological standpoint, ABC-TG is predicted to have an electric field tunable band gap up to 0.3 eV,[10,12] which is attractive for optoelectronic applications such as infrared photodetectors. Demonstrating control of the

band gap and understanding the transport properties of gapped ABC-TG are critical to realize these applications. Although a tunable band gap in ABC-TG has been demonstrated by infrared absorption spectroscopy,[16] transport characteristics are less well-established and limited to small electric fields.[14,22] In stark contrast to ABC-TG, the energy dispersion of ABA-trilayer graphene (ABA-TG) consists of both monolayer-like and bilayer-like subbands.[9] Interestingly, both subbands become massive due to remote hopping processes allowed by mirror symmetry with respect to the middle layer,[9] though ABA-TG remains gapless. Most studies to date have focused on ABA-TG's unique Landau level structures in a magnetic field.[17,20,21,23] ABA-TG has been shown to remain metallic upon the application of a perpendicular electric field but little is known beyond that.[7,14,20] Multiple bands contribute to charge transport in ABA-TG even close to the charge neutrality point. The characteristics of these bands, and in particular their

evolutions in a perpendicular electric field, are still poorly understood.

In this work, we report on the transport properties of ABC-TG and ABA-TG using dual locally gated field effect devices. By controlling the displacement field D and the carrier density n independently over a wide range using the two gates, we demonstrate unambiguously the opening of a band gap in ABC-TG, where the resistance at the CNP increases by 5 orders of magnitude with increasing D. Furthermore, our measurements suggest a saturation of the band gap at $D \sim 3.0$ V/nm, in agreement with a tight-binding calculation that takes Hartree screening into account self-consistently.[12] In ABA-TG, the signatures of two-band conduction are observed for the first time. The onset carrier density as a function of D is compared to a self-consistent Hartree theory. The agreement between experiment and theory is satisfactory; we argue that the discrepancy is likely due to an inadequate treatment in the simplified calculations of the occupied sigma bands and of exchange interactions.

The procedures used to fabricate the dual-gated devices are described in the Supporting Information. Briefly, we first pattern local bottom gate stacks of 28 nm HfO_2 film and 30 nm Au on SiO_2/doped Si substrate using optical lithography, reactive ion etching, metal deposition, and atomic layer deposition of HfO_2. Graphene sheets are then mechanically exfoliated to the local gate area using bulk graphite (ZYA grade, distributed by SPI). A TG piece is first identified by its optical contrast and confirmed by Raman spectroscopy using the profile of its 2D band[15] (Figure 1b). Hall bar-like devices are
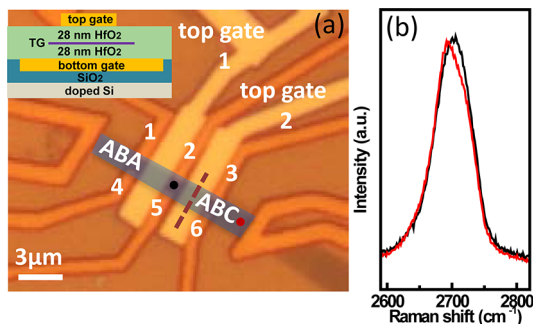

Figure 1. Device layout and Raman spectra. (a) An optical micrograph of the dual gated trilayer graphene device. The blue shaded area represents the trilayer flake. The six voltage probes and two top gate electrodes are marked on the graph. The local bottom gate is not visible in this image. The dashed line marks a schematic location of the domain boundary between the ABA and ABC stacked portions of the flake. Inset: a schematic of the cross section. (b) Raman spectra of the 2D band taken at the black and red spots marked in a, respectively. The black trace shows the profile of an ABA-TG and the red trace shows that of an ABC-TG.

made by e-beam lithography. After the deposition of metal electrodes, another 28 nm thick HfO_2 film is deposited on top of the device as the top gate dielectric, followed by the patterning and deposition of local top gate electrodes. Both HfO_2 layers are grown by atomic layer deposition using the recipe previously described in ref 24. An optical micrograph of a finished device is shown in Figure 1a, together with a schematic of the device as the inset. Micro Raman spectra along the length of the device reveals that it consists of ABA-TG and ABC-TG regions separated by a domain boundary under top gate 2. The two corresponding 2D band profiles are shown in Figure 1b.

This identification is further supported by resistance measurements using different pairs of voltage probes (Figure 1a) and described in detail later. This unique geometry enables us to directly compare the transport properties of TG samples with different stacking orders on the same device.

Both the top and the bottom HfO_2 gates exhibit a gating efficiency of $\sim 5.5 \times 10^{12}$ cm^{-2}/V, as deduced from the sample's quantum Hall sequence at a fixed magnetic field. This is approximately 80 times higher than the commonly used SiO_2 global back gate. The breakdown voltages of both gates are greater than 8 V. The large capacitance and high breakdown voltage of the two gates allow us to vary the perpendicular displacement field D and the carrier density n independently over exceedingly large range with $|D|$ up to 6 V/nm and n up to 3.3×10^{13}/cm^2 in experiments reported here, thereby probing regimes unexplored in previous studies limited to $|D| \leq 1$ V/nm.[7,13,14,17,18,20,22] We measure the resistance R between different pairs of voltage probes in the temperature range of 1.5–200 K while varying the top and bottom gate voltages V_{tg} and V_{bg}. Both four-terminal standard lock-in techniques and two-terminal DC techniques are used to measure the resistances as they vary by 6 orders of magnitude in different parts of the device. We estimate the carrier mobility to be about 1000 cm^2/(V s). The technical details are given in the Supporting Information.

Figure 2a plots the resistance between probes 2 and 3, R_{23} (V_{tg}) at $T = 1.5$ K, as a function of sweeping V_{tg} from −5.2 to 5.8 V on top gate 2 and at fixed V_{bg}'s ranging from −4.0 to 5.0 V in 0.5 V steps. The respective displacement field of the top and bottom gate (+ for top and − for bottom) $D_{tg,bg} = \pm$

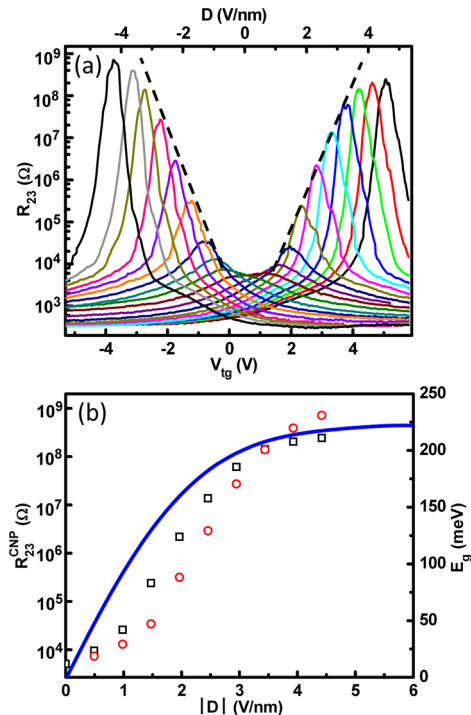**Figure 2.** Transport characteristics of the ABC-TG. (a) Semilog plot of R_{23} as a function of V_{bg} and V_{tg}. From left to right, V_{bg} changes from 5.0 V to −4.0 V in 0.5 V steps. The top axis marks the average D at the CNPs. The dashed lines are guide to the eye. $T = 1.5$ K. (b) Left axis: Semilog plot of the CNP resistance R_{23}^{CNP} as a function of $|D|$. Black squares are from positive D's, and red circles are from negative D's. Right axis: Theoretical band gap $E_g(D)$ of ABC-TG from ref 12.

$\varepsilon(V_{tg,bg} - V^0_{tg,bg})/d$, where the HfO$_2$ film thickness $d = 28$ nm is obtained with atomic force microscopy and its dielectric constant $\varepsilon = 28$ is calculated using the charging efficiency of the gates. $V^0_{tg} = 1.0$ V and $V^0_{bg} = 0.5$ V are due to the unintentional chemical doping from the environment. Similar to bilayer graphene, the maximum of each trace in Figure 2a corresponds to a charge neutrality point (CNP), where $n \sim (D_{tg} - D_{bg}) = 0$. As the average perpendicular field through the trilayer $D = (D_{tg} + D_{bg})/2$ increases from 0 to ± 4.5 V/nm, R_{23} at the CNP increases dramatically by 5 orders of magnitude from 6000 Ω to several hundred MΩ. Although R_{23} consists of both ABA-TG and ABC-TG, the dramatic gate dependence originates from that of the ABC portion (see Figure 3 and Supporting
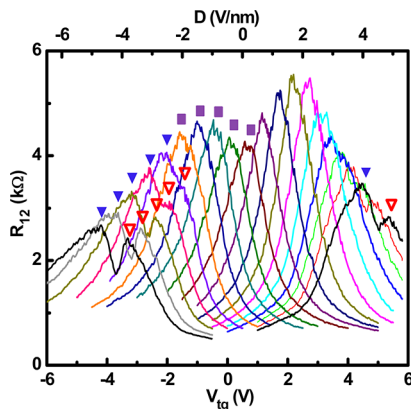

Figure 3. Transport characteristics of the ABA-TG. R_{12} as a function of V_{bg} and V_{tg}. From left to right, V_{bg} changes from 5.0 V to -4.0 V in 0.5 V steps. $T = 1.5$ K. The red triangles mark the CNPs. The blue triangles mark the top of the second valence band. The purple squares mark the merged peak. See the main text for explanations.

Information for more discussion). Away from the CNP, R_{23} sharply decreases to a few hundred Ω as the carrier density n increases. The ratio between the resistance of the "on" state at high carrier density and the "off" state at the CNP reaches 10^6 at large $|D|$, which is the largest ratio reported for trilayer graphene. The observed gate dependence of R_{23} unambiguously demonstrates the opening of a band gap in the ABC-TG portion of the device.

Figure 2a also reveals an interesting trend of the CNP resistance with increasing $|D|$. As the dashed lines in Figure 2a show, the CNP resistance follows an approximate exponential dependence on $|D|$ at small fields but deviates at $|D| > 3.0$ V/nm. This trend is more clearly seen in Figure 2b, where we plot R^{CNP}_{23} vs $|D|$ in a semilog plot (left axis). Also plotted there (right axis) is the calculated band gap E_g in ABC-TG using a density functional theory.[12] For $|D| > 1$ V/nm, where studies of bilayer graphene suggest[25] that E_g is likely to be no longer dominated by disorder, $\ln(R^{CNP}_{23})$ and E_g have similar dependences on $|D|$. Both increase roughly linearly with $|D|$ until $|D|$ reaches approximately 3 V/nm, where a tendency toward saturation is seen both in theory and in experiment. Although a quantitative relation between R^{CNP}_{23} and E_g is difficult to establish due to the complicating role of disorder, the saturation of R^{CNP}_{23} at large $|D|$ is consistent with the saturation of the band gap. In the Supporting Information, we demonstrate the saturation of R^{CNP}_{23} is not due to parasitic resistance or heating effects and other relevant energy scales related to E_g also saturate with increasing $|D|$. Together, these

are the first experimental indications of the saturation of E_g in ABC-TG.

The D-dependence of the transport properties of the ABA portion of our device is drastically different. Figure 3 plots the resistance between probes 1 and 2, $R_{12}(V_{tg})$ at $T = 1.5$ K as a function of V_{bg} and V_{tg} on top gate 1, using the same voltage range and interval as in Figure 2a. R_{12} measures the ABA-TG only. In stark contrast to the drastic increase of R^{CNP}_{23} in the ABC-TG with $|D|$, the maxima of $R_{12}(V_{tg})$, R^{max}_{12} is several kΩ. This observation unambiguously demonstrates the lack of an electric field-induced band gap in ABA-TG, in agreement with previous experiments[7,14,20] and the theoretical expectation[9] of a semimetallic band structure for this stacking order.

Figure 3 also reveals several interesting features not seen in previous studies of dual-gated ABA-TG.[7,14,20] R^{max}_{12} of each curve (marked by blue triangles and purple squares) first increases with increasing $|D|$, although this increase is much smaller than that of the ABC-TG over the same range, then reaches a global maximum near $|D| = 2$ V/nm, and eventually decreases with further increase of $|D|$. Furthermore, in conjunction with the decrease of R^{max}_{12} at large $|D|$, a "side" peak starts to develop. This new peak, marked by red triangles in Figure 3, occurs for both negative and positive D's and appears always to the right side of R^{max}_{12}.

To elucidate the origins of the two peaks, we plot in Figure 4a V_{tg} and V_{bg} of the marked positions in Figure 3 (red triangles, blue triangles, and purple squares). Surprisingly, the "side" peaks marked by the red triangles follow a straight line of slope one (the dashed line in Figure 4a), which also coincides with the $V_{tg}-V_{bg}$ line of the CNPs on the ABC portion of the device. In another word, the "side" peaks in Figure 3 *actually* correspond to the CNPs of the ABA-TG, contrary to the intuition of associating R^{max}_{12} with the CNP. The position of R^{max}_{12} (blue triangles) itself increasingly deviates from the CNP line as $|D|$ increases. At $|D| < 2.5$ V/nm, only one resistance maximum is perceptible, as marked by the purple squares in Figure 4a. It appears that the nonmonotonic dependence of R^{max}_{12} on D originates from the development of the two peaks.

The characteristics of $R_{12}(V_{tg})$ at large $|D|$ are reminiscent of two-band conduction observed in GaAs/GaAlAs heterostructures[26] and more recently in bilayer graphene.[27] In a 2D system with more than one subband, as E_F approaches the band edge of the higher subband, additional scattering channels become available, causing resistance to increase. As E_F further increases, carriers occupy the higher subband and participate in both screening and conduction; these effects cause the total resistance to drop again. This process results in a "negative differential resistance" (NDR) region, which appears in the transfer curves shown in Figure 3, to the right side of the blue triangles.

A similar two-band conduction model that takes into account the evolution of ABA-TG bands in a perpendicular D field provides a natural explanation for the appearance and evolution of the two resistance peaks observed in Figure 3. This situation is illustrated in Figure 4b and c, where we plot the four low energy bands of ABA-TG for $U_{SCR} = 0$ and $U_{SCR} = 160$ meV, respectively, using a tight-binding model with the hopping parameters as follows:[17] $\gamma_0 = 3$ eV, $\gamma_1 = 0.4$ eV, $\gamma_2 = -0.028$ eV, $\gamma_3 = \gamma_4 = 0$, $\gamma_5 = 0.05$ eV, and $\delta = 0.046$ eV. Here, U_{SCR} is the screened potential difference between the top and the bottom layers of the ABA-TG. As D increases, so do U_{SCR} and the splitting of the higher energy subbands as shown in Figure 4b and c. Starting from the CNP (dashed lines in Figure 4b and c),
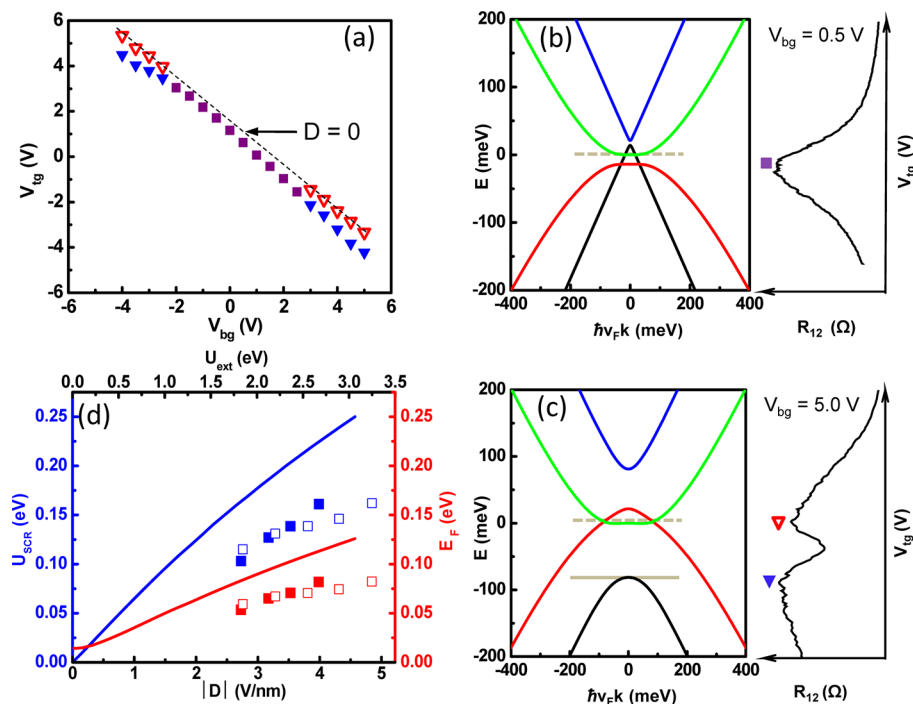
Figure 4. Two-band conduction in the ABA-TG. (a) Positions of R_{12} peaks marked in Figure 3 in a V_{tg} vs V_{bg} plot. The dashed line corresponds to slope 1 and coincides with the CNP line of the ABC portion of the device. (b and c) The low-energy bands of ABA-TG obtained using a tight-binding model with $U_{SCR} = 0$ meV (b) and $U_{SCR} = 160$ meV (c). $R_{12}(V_{tg})$ data from Figure 3 are plotted on the side to qualitatively illustrate the resistance change with changing E_F. The symbols follow Figure 3. The gray dashed lines in b and c mark the CNP, and the gray solid line in c marks the edge of the second valence band. (d) U_{SCR} (left axis) and E_F (right axis) as a function of $|D|$ (bottom axis) and U_{ext} (top axis) obtained by fitting experimental data (symbols) and from self-consistent Hartree screening calculations (lines). Solid squares are from positive D's and hollow squares are from negative D's.

E_F moves downward as V_{tg} becomes more negative and more holes are added. Consequently, R_{12} decreases. As E_F approaches the second valence band, increased scattering causes R_{12} to turn around and increase until the second valence band is populated and the added conduction channel causes R_{12} to drop again. Thus, we associate the blue triangles with E_F reaching the top of the second valence band, as illustrated in Figure 4c using the corresponding experimental curve. The width of the NDR region is controlled by charge disorder, which produces localized states near the band edges and also smears their positions.[28,29] This disorder broadening of subbands also causes the merge of the two resistance peaks at small field $|D| < 2.5$ V/nm in Figure 3 (Figure 4b), where the band splitting is too small to be resolved.[25,28−30] Interestingly, we did not see evidence of NDR occurring at the bottom of the second conduction band. This is likely due to the fact that this band evolved from a monolayer-like band and has a much smaller density of states available for scattering, whereas the top of the second valence band evolved from a bilayer-like band with large density of states.

To quantitatively compare our experiment with the commonly used self-consistent Hartree theories, we use the experimentally measured carrier density at R_{12}^{max} to deduce the screened U_{SCR} in the tight-binding model[11,12] which yields the population of that second valence band at the carrier density. The resulting U_{SCR} (blue symbols) and the E_F (red symbols) are plotted in Figure 4d vs the $|D|$ at R_{12}^{max} (bottom axis), and the unscreened external potential difference $U_{ext} = 2de|D|$ (top axis), where $d = 0.335$ nm is the interlayer spacing of trilayer. Also plotted there are U_{SCR} (blue solid line) and E_F (red solid line) obtained in our self-consistent Hartree theory with the

tight-binding parameter values cited earlier. Here the calculations use self-consistent Hartree screening to solve for U_{SCR} and E_F required to populate the second valence band at the U_{ext} given by experiment. Screening by the remote sigma bands not included in our calculation is modeled by a fixed dielectric constant $\varepsilon = 4$.

Overall, the theory results qualitatively reproduce the experimental trend of screening very well, although the calculated values of U_{SCR} and E_F are larger by ~30%. Varying the tight binding parameters will change both the calculated and the experimentally determined U_{SCR}, but in similar fashions that will not reduce the discrepancy. Experimentally, disorder broadening hinders a precise determination of the band edges. This uncertainty does not appear to be large enough to explain the discrepancy. Theoretically, the overestimate of U_{SCR} might be attributed to an underestimate of screening. This could originate from the inadequate treatment of the sigma bands, whose role in polarization is more complex and could be stronger than our phenomenological $\varepsilon = 4$ effect.[16,31] Our neglect of exchange energies may also have an effect. Our experiment provides the first data set in ABA-TG to which theoretical calculations may be compared.

In summary, we report on the electrical transport of dual-gated ABA and ABC trilayer graphene in exceedingly large perpendicular electric fields. Our experiments unambiguously demonstrate the opening of a large transport band gap in ABC-TG, where the resistance changes by 6 orders of magnitude. Our data suggest the band gap saturates at $|D| \sim 3$ V/nm. In ABA-TG, we observe signatures of two-band conduction at large D. Tight-binding calculations using self-consistent Hartree screening can explain the observations qualitatively but reveal

quantitative discrepancies which motivate further theoretical work.

■ ASSOCIATED CONTENT

Ⓢ Supporting Information

Device fabrication procedure, measurement techniques, and additional evidence of band gap saturation in ABC-TG. This material is available free of charge via the Internet at http://pubs.acs.org.

■ AUTHOR INFORMATION

Notes

The authors declare no competing financial interest.

■ ACKNOWLEDGMENTS

■ REFERENCES

(1) Castro Neto, A. H.; Guinea, F.; Peres, N. M. R.; Novoselov, K. S.; Geim, A. K. *Rev. Mod. Phys.* **2009**, *81* (1), 109−162.

(2) Henriksen, E. A.; Eisenstein, J. P. *Phys. Rev. B* **2010**, *82* (4), 041412.

(3) Zou, K.; Hong, X.; Zhu, J. *Phys. Rev. B* **2011**, *84* (8), 085408.

(4) Young, A. F.; Dean, C. R.; Meric, I.; Sorgenfrei, S.; Ren, H.; Watanabe, K.; Taniguchi, T.; Hone, J.; Shepard, K. L.; Kim, P. *Phys. Rev. B* **2012**, *85* (23), 235458.

(5) McCann, E. *Phys. Rev. B* **2006**, *74* (16), 161403.

(6) Zhang, Y. B.; Tang, T. T.; Girit, C.; Hao, Z.; Martin, M. C.; Zettl, A.; Crommie, M. F.; Shen, Y. R.; Wang, F. *Nature* **2009**, *459* (7248), 820−823.

(7) Craciun, M. F.; Russo, S.; Yamamoto, M.; Oostinga, J. B.; Morpurgo, A. F.; Tarucha, S. *Nat. Nanotechnol.* **2009**, *4* (6), 383−388.

(8) Koshino, M.; McCann, E. *Phys. Rev. B* **2009**, *80* (16), 165409.

(9) Koshino, M.; McCann, E. *Phys. Rev. B* **2009**, *79* (12), 125443.

(10) Avetisyan, A. A.; Partoens, B.; Peeters, F. M. *Phys. Rev. B* **2010**, *81* (11), 115432.

(11) Koshino, M. *Phys. Rev. B* **2010**, *81* (12), 125304.

(12) Zhang, F.; Sahu, B.; Min, H.; MacDonald, A. H. *Phys. Rev. B* **2010**, *82* (3), 035409.

(13) Bao, W.; Jing, L.; Velasco, J.; Lee, Y.; Liu, G.; Tran, D.; Standley, B.; Aykol, M.; Cronin, S. B.; Smirnov, D.; Koshino, M.; McCann, E.; Bockrath, M.; Lau, C. N. *Nat. Phys.* **2011**, *7* (12), 948−952.

(14) Jhang, S. H.; Craciun, M. F.; Schmidmeier, S.; Tokumitsu, S.; Russo, S.; Yamamoto, M.; Skourski, Y.; Wosnitza, J.; Tarucha, S.; Eroms, J.; Strunk, C. *Phys. Rev. B* **2011**, *84* (16), 161408.

(15) Lui, C. H.; Li, Z. Q.; Chen, Z. Y.; Klimov, P. V.; Brus, L. E.; Heinz, T. F. *Nano Lett.* **2011**, *11* (1), 164−169.

(16) Lui, C. H.; Li, Z. Q.; Mak, K. F.; Cappelluti, E.; Heinz, T. F. *Nat. Phys.* **2011**, *7* (12), 944−947.

(17) Taychatanapat, T.; Watanabe, K.; Taniguchi, T.; Jarillo-Herrero, P. *Nat. Phys.* **2011**, *7* (8), 621−625.

(18) Zhang, F.; Jung, J.; Fiete, G. A.; Niu, Q.; MacDonald, A. H. *Phys. Rev. Lett.* **2011**, *106* (15), 156801.

(19) Zhang, L. Y.; Zhang, Y.; Camacho, J.; Khodas, M.; Zaliznyak, I. *Nat. Phys.* **2011**, *7* (12), 953−957.

(20) Henriksen, E. A.; Nandi, D.; Eisenstein, J. P. *Phys. Rev. X* **2012**, *2* (1), 011004.

(21) Zhang, F.; Tilahun, D.; MacDonald, A. H. *Phys. Rev. B* **2012**, *85* (16), 165139.

(22) Khodkov, T.; Withers, F.; Hudson, D. C.; Craciun, M. F.; Russo, S. *Appl. Phys. Lett.* **2012**, *100* (1), 013114.

(23) Lee, Y.; Velasco, J.; Tran, D.; Zhang, F.; Bao, W.; Jing, L.; Myhro, K.; Smirnov, D.; Lau, C. N. *arXiv:1210.6592*, **2012**.

(24) Zou, K.; Hong, X.; Keefer, D.; Zhu, J. *Phys. Rev. Lett.* **2010**, *105* (12), 126601.

(25) Zou, K.; Zhu, J. *Phys. Rev. B* **2010**, *82* (8), 081407.

(26) Stormer, H. L.; Gossard, A. C.; Wiegmann, W. *Solid State Commun.* **1982**, *41* (10), 707−709.

(27) Efetov, D. K.; Maher, P.; Glinskis, S.; Kim, P. *Phys. Rev. B* **2011**, *84* (16), 161412.

(28) Nilsson, J.; Castro Neto, A. H. *Phys. Rev. Lett.* **2007**, *98* (12), 126801.

(29) Rossi, E.; Das Sarma, S. *Phys. Rev. Lett.* **2011**, *107* (15), 155502.

(30) Li, Q.; Hwang, E. H.; Das Sarma, S. *Phys. Rev. B* **2011**, *84* (11), 115442.

(31) Siegel, D. A.; Park, C. H.; Hwang, C.; Deslippe, J.; Fedorov, A. V.; Louie, S. G.; Lanzara, A. *Proc. Natl. Acad. Sci. U.S.A.* **2011**, *108* (28), 11365−11369.